A Relative of $Sr_4Fe_6O_{13}$ with Double Perovskite Layers: $Bi_4Sr_{14}Fe_{24}O_{56}$, $m = 2$-Members of a Potential Series $[(Sr,Bi)_2Fe_4O_{7-\delta}][(Sr,Bi)_2Fe_2O_6]_m$

C. Lepoittevin, S. Malo,* M. Hervieu, D. Grebille, and B. Raveau

Laboratoire CRISMAT, UMR CNRS ENSICAEN 6508, 6 bd Maréchal Juin, 14050 CAEN Cedex 4, France

Received August 2, 2004. Revised Manuscript Received September 30, 2004

A new ferrite $Bi_4Sr_{14}Fe_{24}O_{56}$ (i.e., $Bi_{4/3}Sr_{14/3}Fe_8O_{18.66}$) has been synthesized. The high-resolution electron microscopy study of this oxide shows that its modulated structure consists of an original intergrowth of double perovskite layers $[(Sr,Bi)_2Fe_2O_6]$ with oxygen-deficient $[(Sr,Bi)_2Fe_4O_{7-\delta}]$ layers. The latter are closely related to the $[Sr_2Fe_4O_{7-\delta}]$ layers observed in $Sr_4Fe_6O_{13}$, that is, built up of FeO_5 bipyramids and distorted tetragonal pyramids. This new oxide appears as the member $m = 2$ of a potential series $[(Sr,Bi)_2Fe_4O_{7-\delta}]$ $[(Sr,Bi)_2Fe_2O_6]_m$, which offers a great possibility of cationic and oxygen nonstoichiometry, in connection with the structure modulation.

The extraordinary ability of the strontium and bismuth strontium ferrites to form layered structures involving perovskite layers has been demonstrated these last 15 years by the discovery of Ruddlesden and Popper phases $Sr_{n+1}Fe_nO_{3n+1}$,[1−3] of the 1201 ferrite $Bi_{0.4}Sr_{2.5}Fe_{1.1}O_5$,[4−5] of the 2201 ferrites $Bi_{2-x}Sr_{2+x}FeO_6$ with x ranging from 0 to ∼0.9,[6] of the 2212 phases $Bi_{2+x}Sr_{3-x}Fe_2O_{9+\delta}$,[7,8] and of the 2223 ferrite $Bi_2Sr_3Fe_4O_{12}$.[9−10] All of these oxides correspond to the intergrowth of single or multiple perovskite layers with single or double or even triple distorted rock salt-type layers. Besides these compounds, the strontium ferrite $Sr_4Fe_6O_{13}$, synthesized a long time ago,[11] is of interest, due to its original layered structure,[12,13] which also consists of single perovskite layers, but differs from the other layered ferrites by the nature of the iron−oxygen layers sandwiched between the perovskite layers. On the basis of these structural analyses, the intermediate layers have been described as double ribbons of edge-sharing distorted FeO_5 tetragonal pyramids alternating with double ribbons of FeO_5 trigonal bipyramids, according to the 1:1 sequence along $\vec{a}$. Recent papers[14,15] show that this oxide can exhibit an oxygen deficiency, leading to the formulation $Sr_4Fe_6O_{13-\delta}$. Consequently, its structure is modulated and considerably more complex. The amplitude of the modulation vector was clearly correlated to the oxygen stoichiometry.[14]

Bearing in mind the analogy of this structure with that of the RP ferrites and with the bismuth strontium ferrites, we have considered the possibility of existence of a new family of materials, whose structures would involve multiple perovskite layers, instead of singles ones. We have thus investigated the Bi−Sr−Fe−O system, starting from nominal compositions based on such hypotheses. We report herein on a new ferrite, $Bi_4Sr_{14}Fe_{24}O_{56}$, whose original modulated structure is related to that of $Sr_4Fe_6O_{13}$, double perovskite layers replacing the single perovskite layers.

Experimental Section

The powder sample was prepared from a mixture of the starting materials Bi_2O_3, Fe_2O_3, and SrO in a glovebox. The different oxide powders, weighed in the stoichiometric ratio, were ground in an agate mortar, pressed into bars, and sealed in a silica tube. The mixture was heated at 1100 °C for 48 h, with a heating rate of 2 °C/min, and was slow cooled at the same rate.

Single crystals were grown starting from the same mixture (Bi_2O_3, Fe_2O_3, and SrO) as the powder sample, pressed in an alumina crucible, sealed in a silica tube, and then heated according to the following thermal cycle: heating at 1200 °C for 48 h, with a heating rate of 3 °C/min, and slow cooled to

* Corresponding author. Phone: (33)2.31.45.26.10. Fax: (33)2.31.95.16.00. E-mail: sylvie.malo@ensicaen.fr.

(1) Dann, S. E.; Weller, T. M.; Currie, D. B. *J. Solid State Chem.* **1991**, *92*, 237.
(2) Dann, S. E.; Weller, T. M.; Currie, D. B. *J. Solid State Chem.* **1992**, *97*, 179.
(3) Lucchini, E.; Minichelli, D.; Sloccari, G. *Acta Crystallogr., Sect. B* **1973**, 2356.
(4) Pelloquin, D.; Maignan, A.; Hervieu, M.; Michel, C.; Raveau, B. *J. Solid State Chem.* **2000**, *151*, 210.
(5) Allix, M.; Pelloquin, D.; Studer, F.; Nguyen, N.; Wahl, A.; Maignan, A.; Raveau, B. *J. Solid State Chem.* **2002**, *167*, 48.
(6) Pelloquin, D.; Allix, M.; Michel, C.; Hervieu, M.; Raveau, B. *Philis. Mag. B* **2001**, *81*, 1669.
(7) Lepage, Y.; McKinnon, W. R.; Tarascon, J. M.; Barboux, P. *Phys. Rev. B* **1989**, *40*, 6810.
(8) Hervieu, M.; Michel, C.; Nguyen, N.; Retoux, R.; Raveau, B. *Eur. J. Solid State Chem.* **1988**, *25*, 375.
(9) Retoux, R.; Michel, C.; Hervieu, M.; Nguyen, N.; Raveau, B. *Solid State Commun.* **1989**, *69*, 599.
(10) Pissas, M.; Papaefthymiou, V.; Simopoulos, A.; Kostikas, A.; Niarchos, D. *Solid State Commun.* **1990**, *73*, 767.
(11) Kanamuru, F.; Shimada, M.; Koizumi, M. *J. Phys. Chem. Solids* **1972**, *33*, 1169.
(12) Yoshiasa, A.; Ueno, K.; Kanamaru, F.; Horiuchi, H. *Mater. Res. Bull.* **1986**, *21*, 175.
(13) Ohkawa, M.; Fujita, S.; Takeno, S.; Nakatsuka, A.; Yoshiasa, A.; Uchida, M.; Oshumi, K. *Z. Kristallogr.* **1997**, *212*, 848.
(14) Mellenne, B.; Retoux, R.; Lepoittevin, C.; Hervieu, M.; Raveau, B. *Chem. Mater.*, published online October 16, 2004, http://dx.doi.org/10.1021/cm040127d.
(15) Rossell, M. D.; Abakumov, A. M.; Van Tendeloo, G.; Pardo, J. A.; Santiso, J. *Chem. Mater.* **2004**, *16*, 2578.

10.1021/cm048730j CCC: $27.50
Published on Web 11/23/2004

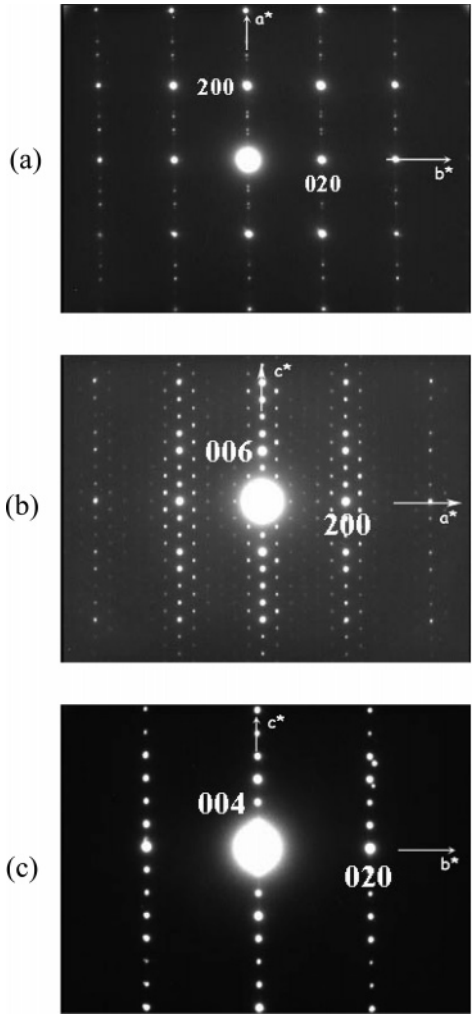

Figure 1. (a) [001], (b) [010], and (c) [100] ED patterns of $Bi_4Sr_{14}Fe_{24}O_{56}$ indexed in a F-type subcell.

1000 °C at a rate of 5 °C/h, and then furnace cooled to room temperature.

The powder X-ray diffraction (PXRD) analyses were carried out at room temperature with a Philips diffractometer working with the Cu Kα ($\lambda = 1.506$ Å) in the range $10° \leq 2\theta \leq 110°$.

The oxygen content was determined by chemical analyses. The sample was studied by transmission electron microscopy. For this work, a small piece of sample was crushed in a mortar containing alcohol, and then a droplet was deposited on a copper grid covered with holey carbon film. Electron diffraction was carried out with a JEOL 200 CX electron microscope equipped with an eucentric goniometer (±60°). High-resolution electron microscopy (HREM) was carried out with a TOPCON 002B microscope equipped with a ±10° double tilt ($V = 200$ kV, $Cs = 0.4$ mm). Image calculations were carried out with the MacTempas software. Both microscopes are equipped with an energy dispersive spectroscopy (EDS) analyzer. The magnetic measurements were performed on a SQUID magnetometer ($T < 400$ K) and a Faraday balance (300 K < T < 800 K).

Results and Discussion

Electron Diffraction and Powder X-ray Diffraction. The electron diffraction study coupled with EDS analysis carried out on numerous microcrystals of a sample of nominal composition $Bi_2Sr_7Fe_{12}O_{28-\delta}$ allowed the very homogeneous cationic composition "$Bi_2Sr_7Fe_{12}$" to be confirmed. The reconstruction of the reciprocal space from the [001], [010], and [100] ED patterns (Figure 1) shows that a first set of intense reflections

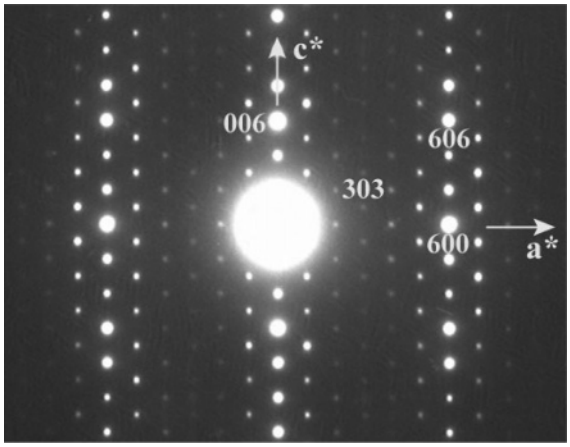

Figure 2. [010] ED pattern indexed in the B-type supercell with $a \approx 3a_p\sqrt{2}$, $b \approx a_p\sqrt{2}$, and $c \approx 26$ Å.

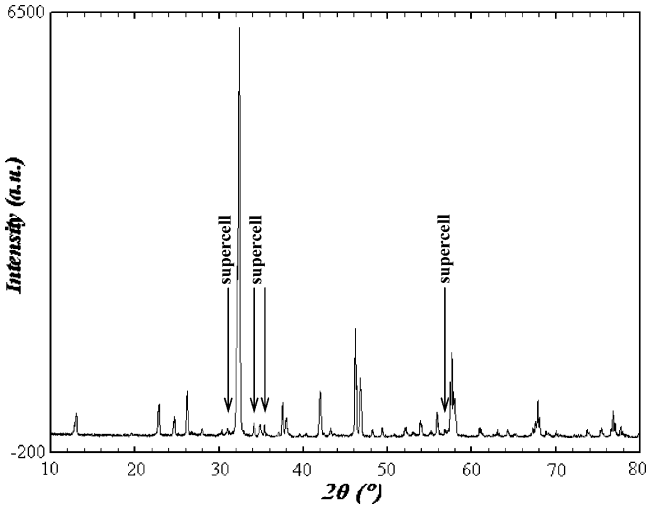

Figure 3. Powder X-ray diffraction data for $Bi_4Sr_{14}Fe_{24}O_{56}$. Arrows marked the superstructural peaks.

can be described in an orthorhombic sub-cell with $a \approx b \approx a_p\sqrt{2}$ and $c \approx 26$ Å with reflection conditions corresponding to a F lattice with the possible groups $Fmmm$, $Fmm2$, or $F222$. Besides those fundamental reflections, a second set of extra reflections is observed on the [001] and [010] ED patterns (Figure 1a,b), characteristic of a modulated structure. The satellites evidence a modulation vector with two components, $p\vec{a}^* + q\vec{c}^*$. For all of the crystallites studied by ED, the q component of the modulation vector was equal to 1, whereas the average of the p component is $^1/_3$. So, for clarity worries, only the p component of the modulation vector will be reported hereinafter. Bearing in mind the commensurate nature of the modulation, the structure can be described in a supercell $a \approx 3a_p\sqrt{2}$, $b \approx a_p\sqrt{2}$, and $c \approx 26$ Å. The conditions limiting the reflections hkl:$h+l = 2n$, $0kl$:$k = 2n$, and $hk0$:$k = 2n$ are compatible with the $Bb2b$ and $Bbmb$ space groups (Figure 2).

The lattice parameters refined from the powder X-ray diffraction data in the supercell using the $Bb2b$ space group are $a = 16.6100(5)$ Å, $b = 5.5602(2)$ Å, and $c = 27.1310(7)$ Å in agreement with the ED study. Considering the intensity and the number of peaks characteristic of the supercell (Figure 3) and the parameters to refine, the PXRD data were not sufficient for refining an accurate structural model using the Rietveld method.

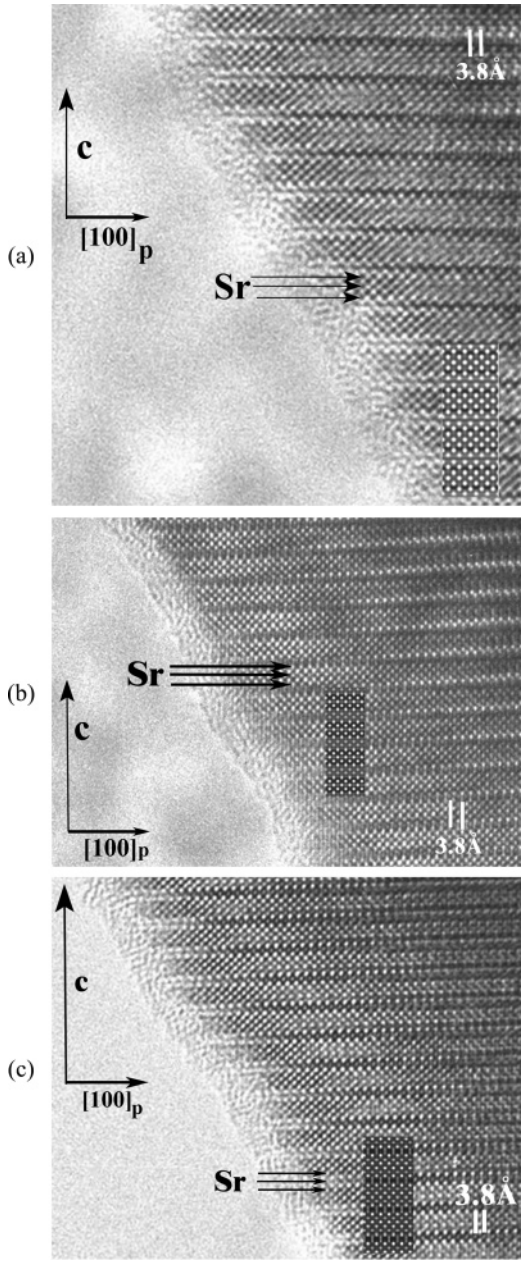

Figure 4. [130] HREM images for $Bi_4Sr_{14}Fe_{24}O_{56}$ recorded with focus values close to (a) −250 Å, (b) −550 Å, and (c) −1150 Å. The theoretical images are shown as insets.

Structural Model by High-Resolution Electron Microscopy. $\{100\}_p$ has been shown a very efficient viewing direction for determining the stacking sequence of the intergrowth structures, as in the RP phases, superconducting cuprates, and derivatives.[4,5,16] In the present phase, the [130] direction is the equivalent one. Three images, picked out from the focus series, are given in Figure 4. Focus values are estimated to −250 (close to Scherzer), −550, and −1150 Å, respectively. In Figure 4a (focus ≈ −250 Å), the zones of high electron density are imaged as darker spots, and the contrast characteristic of perovskite-type derivatives is clearly observed, in the form of five rows spaced by about 1.9 Å (i.e., $\sim a_p/2$) along $\vec{c}$, made of staggered dark spots separated by bright spots. The dark spots

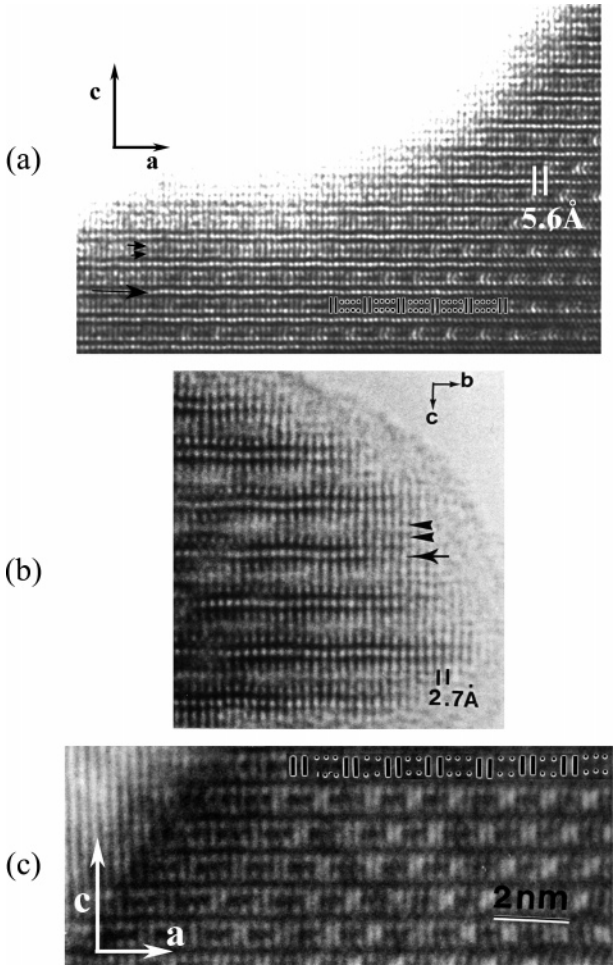

Figure 5. (a) [010] HREM image of $Bi_4Sr_{14}Fe_{24}O_{56}$, (b) [100] HREM image of $Bi_2Sr_3M_2O_8$, and (c) [010] HREM image of $Sr_4Fe_6O_{13}$.

are associated to the strontium and iron positions of the perovskite-like layers. These positions appear as the bright dots in Figure 4b (focus ≈ −550 Å) and in Figure 4c (focus ≈ −1150 Å), where the high electron density zones are highlighted. These groups of bright dots are separated by a double row of staggered gray dots, spaced by about 1.5 Å along $\vec{c}$, associated to a double row of iron atoms. These HREM images fit with those expected for a structure built from the intergrowth of double perovskite and $[Sr_2Fe_4O_{7-\delta}]_\infty$-type layers, the latter being derivative from the rock salt-type layers.

The [010] HREM images (Figure 5a), which are equivalent to the $\{110\}_p$ ones, can be compared to those previously observed for $Bi_2Sr_3M_2O_8$-type (2212) compounds and for $Sr_4Fe_6O_{13-\delta}$,[14] as illustrated in Figure 5b and c. Note that the three structures are modulated along one of the equivalent $\{110\}_p$. The relative positions of the [SrO] layers are similar in our compound (Figure 5a) and the 2212's (Figure 5b); the [SrO] layer sandwiched between two octahedral iron layers is indicated by one black arrow. The two structures mainly differ by the contrast at the level of the rock salt block: first, by the thickness of this rock salt block (the difference > 2 Å being drastic) and, second, by the brightness of the spots associated to the cation positions in the two medium [AO] layers sandwiched between the two [SrO] layers (indicated by two arrowheads in Figure

(16) Hervieu, M.; Pelloquin, D.; Michel, C.; Caldés, M. T.; Raveau, B. *J. Solid State Chem.* **1995**, *118*, 227.

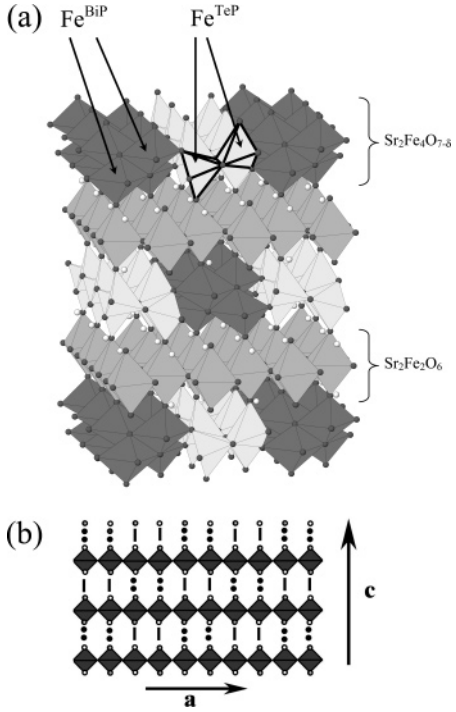

Figure 6. (a) Structural model of $Sr_4Fe_6O_{13}$ and (b) schematically ideal model of $Sr_4Fe_6O_{13}$ ($p = 0.5$).

5a and b). The two bismuth layers of the 2212's are brighter and more spaced out.

The similarity with $Sr_4Fe_6O_{13-\delta}$ (Figure 5c) lies in the nature of the modulation, the contrast at the level of these two medium layers. The contrast at the level of these pyramidal layers in the oxide $Sr_4Fe_6O_{13-\delta}$ (Figure 5c) is mainly based on the 1:1 alternance along $\vec{a}$ of two bright sticks spaced by 2.9 Å with two less bright sticks spaced by 3.4 Å, triple bright sticks appearing additionally which are distributed in a modulated manner according to the $p = 0.47$ modulation vector.[14] In fact, the contrast within the pyramidal layers is different in the present oxide. The sequence along $\vec{a}$ (Figure 5a) consists of two bright sticks spaced by 2.9 Å, alternating with quadruple less bright sticks spaced by 3.4 Å, leading to a tripling of the a parameter (indicated by white symbols in the image). From these observations, it clearly appears that the modulation of the structure at the level of the rock salt block of this new phase can be deduced from the structure of $Sr_4Fe_6O_{13}$ (Figure 6a). In the perfectly stoichiometric $Sr_4Fe_6O_{13}$, one double $[Fe_2]_\infty^{BiP}$ ribbon of edge-sharing FeO_5 trigonal bipyramids alternates with one double $[Fe_2]_\infty^{TeP}$ ribbon of edge-sharing distorted tetragonal FeO_5 pyramids along $\vec{a}$ (Figure 6a), corresponding to a modulation vector $p = 0.50$. These structural characters are schematically drawn in Figure 6b for a simple reading. As one oxygen deficiency is created from time to time in the $Sr_2Fe_4O_{7-\delta}$ slice, a double $[Fe_2]_\infty^{TeP}$ ribbon is replaced by a triple ribbon of edge-sharing FeO_5 polyhedra. In fact, this phenomenon takes place, according to a modulated periodicity along $\vec{a}$ ($p = 0.47$). In the case of $Sr_4Fe_6O_{13-\delta}$, we have previously shown that p was related to δ by the expression $p = (1 - \delta)/2$.[14] Thus, considering that in this new phase, double perovskite layers $[(Sr,Bi)_4Fe_4O_{12}]_\infty$ replace the single perovskite layers $[Sr_2Fe_2O_6]_\infty$, and that the oxygen deficiency originates from the $[Sr_2Fe_4O_{7-\delta}]_\infty$ alone, this oxide can be formulated

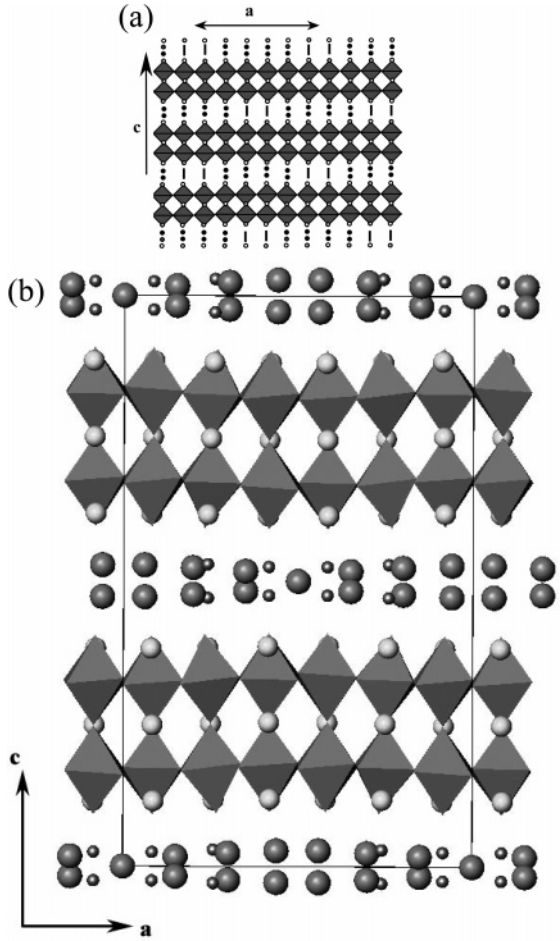

Figure 7. (a) Schematically ideal model of $Bi_4Sr_{14}Fe_{24}O_{56}$ and (b) structural model of $Bi_4Sr_{14}Fe_{24}O_{56}$.

$Bi_{4/3}Sr_{14/3}Fe_8O_{19-\delta}$ with $\delta = 1/3$, because $p = 1/3$ (i.e., $Bi_4Sr_{14}Fe_{24}O_{56}$), in agreement with the redox titration which indicates that practically the totality of iron is trivalent.

The ideal structural model of $Bi_4Sr_{14}Fe_{24}O_{56}$ can then be described as the stacking along $\vec{c}$ of one double perovskite layer $(Sr,Bi)_4Fe_4O_{12}$ with an oxygen-deficient $[(Sr,Bi)_2Fe_4O_{7-\delta}]_\infty$ layer. In the $[(Sr,Bi)_2Fe_4O_{7-\delta}]_\infty$ layer, one double ribbon of trigonal bipyramids $[Fe_2]_\infty^{BiP}$ alternates with one quadruple ribbon of distorted pyramids, along $\vec{a}$, explaining the tripling of the "a" parameter; this ideal model is schematically drawn in Figure 7a, to be compared to Figure 6b.

Preliminary XRD investigation of a single crystal of this new phase allows one to confirm the general structural features of the above ideal model, but shows that the coordination of iron in the $[(Sr,Bi)_2Fe_4O_{7-\delta}]_\infty$ layer is actually more complex than that proposed in this simple model. Especially, it appears that FeO_4 tetrahedra are formed besides the FeO_5 trigonal bipyramids and FeO_5 tetragonal pyramids. The accurate structure of these $[(Sr,Bi)_2Fe_4O_{7-\delta}]_\infty$ layers and the linking of the iron polyhedra will be detailed elsewhere. The theoretical image calculations were carried out starting from the ideal positions deduced from our model (Figure 7b) and the first results of the single-crystal X-ray diffraction refinements. The calculated images are inserted with the [130] experimental images. They fit with the experimental images through focus series, confirming their interpretation and the proposed model.

The contrast associated with the FeO_5 trigonal bipyramids is translated by $(\vec{a} + \vec{c})/2$ between two successive $[(Sr,Bi)_2Fe_4O_{7-\delta}]_\infty$ layers, in agreement with the B centering of the supercell. Such a disposition of the trigonal bipyramids allows one to decrease the strains in the structure. It can be seen also that the flexibility of the double perovskite layer allows one to accommodate the waving of the layers.

Concluding Remarks

From these results, it appears that a new family can be predicted, which derives from the $Sr_4Fe_6O_{13-\delta}$ series, as was recently evidenced,[14] by replacing the single perovskite layers by double perovskite layers. This potential new family can be formulated $[(Sr,Bi)_2 Fe_4O_{7-\delta}]\cdot[(Sr,Bi)_2Fe_2O_6]_m$, where m represents the number of perovskite layers. For the $m = 2$ member, oxygen stoichiometry is able to generate different phases by varying the sequence of double ribbon of trigonal bipyramids and distorted pyramids. In this series, $(Sr,Bi)_6Fe_8O_{19}$ represents the limit member which corresponds to the replacement in $Sr_4Fe_6O_{13}$ (Figure 6a) of single perovskite layers by double perovskite layers.

These considerations suggest that this structural family offers a large possibility to accommodate a variation of oxygen stoichiometry. The detailed high-resolution electron microscopy study of different samples of nominal composition $Bi_4Sr_4Fe_{24}O_{56-\delta}$ confirms this viewpoint.

CM048730J